

https://doi.org/10.1038/s40494-025-01982-7

Microstructures and electrochemical corrosion behaviors of bronze mirror

Check for updates

Minghao Jia¹, Hao Xu², Pei Hu³ & Gang Hu²⊠

Some of the archaeological bronze mirrors retain a smooth silver-gray luster but lack reflective functionality. A high-tin bronze mirror of Western Han Dynasty (202 BC-8 AD) which only showed basic polishing marks without any coating. The silver-gray luster area was the oxidized tin-rich $\alpha + \delta$ eutectoid remaining after the loss of copper in α phase. Microscopic roughness causes light scattering, which is hard to normally reflect clear images. The polishing and copper loss could expose more tin area and form a dense oxide layer that enhances corrosion resistance by blocking active sites and isolating the bronze matrix. Even after thousands of years, mirror surface showed better charge-transfer resistance (R_{ct}) and polarization resistance (R_{p}) than unpolished decorated surface, with max differences approximately 3 times and 5 times, respectively. Patina growth forms corrosion paths, destroying the resistance of the tin-rich surface, especially under green malachite.

Corrosion is the main cause of the deterioration of metal artifacts. For unearthed metal artifacts, the environment contains a mixture of various soluble electrolytes and soil particle impurities, which could adhere to the metal surface. They accumulate and form an uneven oxide layer at the interface between the metal and the external environment. That is, the rust or patina that appears on the surface of the artifacts. Under the natural state of long-term burial, electrochemical corrosion is extremely common¹. It is generally believed that unearthed metal artifacts that have been buried for several years are gradually damaged or decayed by the erosion of various factors in the burial environment, such as water, oxygen, various anions and cations, and microorganisms in the soil, which is often called "corrosion" or "mineralization"². The phenomena such as loosening, crumbling, cracking, splitting, and layered peeling of the surface corrosion layer are common corrosion diseases of unearthed metal artifacts in the whole world at present^{3,4}. Therefore, the protection research of ancient metal artifacts ultimately aims to inhibit or delay the damage or even disintegration of the mechanical structure of the metal caused by the ubiquitous electrochemical corrosion. Conservationists can help artifacts be preserved stably for a long time and retain their academic research value to the greatest extent through the corrosion mechanism5.

Scientific protection requires a comprehensive understanding of various information about the artifacts and testing with multiple technologies, which is crucial for the rational conservation of metal artifacts. The basic work of artifact testing is to first detect the alloy element⁶, the metallographic structure⁷, and the rust composition of the artifact⁸. For example, using techniques such as Fourier transform infrared spectroscopy (FT-IR)⁹ or ion chromatography (IC)^{10,11} to prove that the chloride in the corrosion

products of iron and bronze artifacts is one of the important factors accelerating the pitting deterioration of the metal. The effective detection of chloride ions directly guides the direction of protection work, such as cleaning and desalination operation. Through micro-Raman spectroscopy and scanning electron microscopy (SEM) to obtain the ratio of the mass fractions of goethite ($\alpha\text{-FeOOH}$) and lepidocrocite ($\gamma\text{-FeOOH}$) can judge the protection ability of the rust layer to the metal 12,13 . That is, the higher the proportion of goethite, the higher the stability of the rust, and the smaller the induced current and deformation stress caused by the rust transformation 14 . By these technologies, it is easy to analyze the rust or patina components in situ in the micro-area, and let us understand the phase transformation and layer relationship between the corrosion products under specific conditions, thus inferring the corrosion mechanism of archeological metal.

However, it is quite difficult to break free from the inherent limitations. As for the metal itself covered by mixed rust or patina, it is rather difficult to obtain unified trending on some important corrosion parameters, such as electrochemical current and potential, only through physical phase analysis. The patina surfaces of the archeological artifacts are more complex than the laboratory-simulated samples. Although modern industrial technology can approximately simulate and reproduce the composition and structure of ancient metals, the real manufacturing process and the corrosion state exposed to natural conditions for hundreds of years cannot be replicated by any laboratory at present. In addition to the different chemical compositions of the corrosion products of bronze artifacts, their appearances and structures are also diverse. Even the same corrosion product also exhibits different macroscopic structural characteristics on different artifact surfaces, such as azurite, malachite, and cerussite^{15,16}. There must be local corrosion

¹Key Laboratory of Archaeological Sciences and Cultural Heritage, Institute of Archaeology, Chinese Academy of Social Sciences, Beijing, China. ²School of Archaeology and Museology, Peking University, Beijing, China. ³Key Scientific Research Base of Science & Technology Evaluation, National Cultural Heritage Administration, Beijing University of Chemical Technology, Beijing, China. —e-mail: ganghutg@163.com

differences on the metal matrix covered by them. This is the information that must be clarified in the protection of ancient metal artifacts. How to measure the real electrochemical differences in the corrosion status of the metal covered by patina is of great significance for understanding the microarea corrosion mechanism of bronze and guiding protection operation.

Small and deep corrosion pits often appear on the interface of metal artifacts, even covered with patina, which are generally referred to as pitting corrosion. This is usually due to the relatively high concentration of corrosive ions such as chloride ions in the local rust or patina, or the existence of tiny defects on the metal surface, causing corrosion to occur preferentially in these areas 17,18. On the unearthed bronze artifacts, especially in the depression of some decorated patterns or at the casting defects, corrosive electrolytes are likely to accumulate, thus leading to the occurrence and spread of pitting corrosion. Furthermore, corrosion is likely to occur when there are phase interfaces between different parts of metal artifacts or existing heterogeneous metals. Generally, at the joints, inlaid parts or folded areas of bronze artifacts, the local corrosion zones or bands are prone to form¹⁹. Under the action of local galvanic couples, oxidation corrosion begins to occur at the interface, forming narrow bands or gaps. Corrosive ions are easily trapped inside these areas, resulting in a relatively high ion concentration, which causes the interfaces to corrode preferentially and the local corrosion current to increase^{20,21}. Therefore, conducting a more comprehensive analysis of the local patina and in situ electrochemical corrosion is highly beneficial for understanding various corrosion differences in metal artifacts. It is also essential for the rational implementation of conservation work.

Electrochemical detection in the field of metal artifacts can help obtain thermodynamic and kinetic data related to corrosion reaction. They reflect the tendency and difficulty of degradation reaction, as well as characteristics such as the corrosion rate of metal artifacts, the generation and consumption of intermediate products²². These provide a quantitative basis for evaluating corrosion status and are helpful for an in-depth understanding of the mechanism of corrosion occurrence^{23,24}. Electrochemical testing can largely capture the minute changes in current and potential generated during the corrosion process of metal artifacts and can also uncover the corrosion information of the metal matrix itself hidden beneath the complex patina layers. Among the electrochemical techniques currently applicable to the corrosion of metal artifacts, polarization curves²⁵, electrochemical noise²⁶, square wave voltammetry²⁷ and electrochemical impedance spectroscopy²⁸, etc., are important means. Especially, electrochemical impedance spectroscopy (EIS) may be the most important method for studying oxidized artifacts and evaluating the effects of conservation due to the advantages of its own testing conditions^{29,30}.

It can be understood that for the corrosion of metal artifacts, more attention should be paid to the mechanical properties for immovable artifacts. While for movable artifacts, the focus is more on dealing with local corrosion. Different patina areas should be carried out a comprehensive study on their local corrosion with ancient manufacturing techniques and materials. For example, different processes such as casting, forging, and welding can result in different metallographic structures^{31,32} and chemical compositions^{33,34} of metal artifacts, thereby affecting their corrosion

performance. In addition, surface treatments and coatings during the manufacturing process also have an impact on corrosion. For example, advanced organic acid lead remaining in the mirror mold that could enter the mirror matrix during pouring and gradually precipitate on the surface to show the corrosion degree with different colors³⁵.

Just as a calm lake surface can reflect human figures, the ancients continuously improved the fineness of polishing bronze mirrors to obtain an extremely smooth and regular surface capable of reflecting perfect images. Later, the process of applying coatings to the mirror surface to enhance its reflective ability gradually developed, such as coating with tinmercury alloy³⁶ or some organic wax³⁵. This can be analyzed through the study of the black or silver patina layers on the surface of bronze mirrors. So, did all the bronze mirrors used in ancient daily life undergo the coating process? Moreover, in the bronze mirrors unearthed through archeological excavations or exhibited in collections, there is a phenomenon that parts of the mirror surface still remain shiny. Although they can no longer reflect human figures and have lost their practicality, their smooth, silver-gray luster forms a sharp contrast with the other rough, blue-green patina surfaces

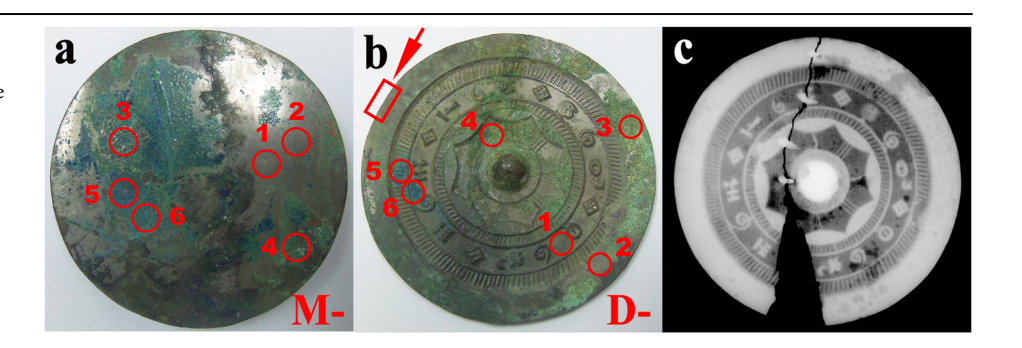
Ancient bronze mirrors not only possess the original and exquisitely cast decorated patterns, but also have smooth and flat surfaces on their mirror sides due to manufacturing process steps such as grinding and polishing. The smooth and flat surface and the cast decorated surface naturally form two original states, which can exhibit two major different corrosion effects on the same artifact in the same burial environment. In this work, bronze mirror was selected as the experimental sample, with different degrees of surface undulation or roughness on both the decorated and the mirror surfaces. From the perspective of in situ corrosion testing, a more comprehensive analysis is conducted to reveal the correlations among the apparent patina, the micro morphology, and the local corrosion, especially the impact of the basic polishing and grinding step on corrosion behavior.

Methods

The artifact sample was a bronze mirror, which was from the Western Han Dynasty (202 BC-8 AD) and is now in the collection of the School of Archaeology and Museology of Peking University. Figure 1 shows the mirror surface (a) and decorated surface (b) of the bronze mirror and the details of the test points for the subsequent experiments. With the aid of X-ray photography, it was shown that the bronze mirror had been broken and mended as shown in Fig. 1c. The restoration report was checked, stating that the soldering material was tin and the mending material was epoxy resin. There were several internal casting defects, which should be bubble cavity formed during casting due to excessive cooling, but have not affected the surface condition of the artifact. In this experiment, the untreated original surface was selected.

The roughness and apparent patina state of the mirror surface and the decorated surface of the bronze mirror were significantly different. The mirror surface was smoother and shinier, with blue and green patina coexisting, and the area of blue patina growth was larger than that on the decorated surface. The decorated surface was rougher, and the whole surface was covered by a thin oxidized layer. The light green patina was distributed

Fig. 1 | Digital and X-ray photos of the bronze mirror. Photos of the mirror (a, b) with the points tested and X-ray photo (c) (The edge pointed by the arrow in (b) is the sampling position of the lateral cross-section measured by SEM-EDS).



over a large area, and the blue patina was present only in small clusters on the left side. Therefore, according to the state of apparent patina, the test points of the mirror surface were divided into three groups: Point 1 and 2 were selected as no obvious patina points or named as smooth area, Point 3 and 4 as light green patina area, and Point 5 and 6 as blue patina area. Similarly, the test points of the decorated surface were also divided into three similar groups. Detailed points could be found as shown in Fig. 1. All the analysis in this work could be focused mainly on these points. Here, M- for the mirror surface and D- for the decorated surface are used as abbreviations.

Microscopy

An ultra-depth-of-field three-dimensional microscope (VHX-2000, Keyence, Japan) was used to observe the roughness of the surface and the appearance of patina. The mirror was stably placed on the microscope stage for point-by-point observation, and images were collected at $\times 100$ magnification.

X-ray imaging

X-ray imaging analysis was performed using the SMART 300HP X-ray machine with tube voltage range of $100\,\mathrm{kV}$ and tube current of $4.0\,\mathrm{mA}$. The imaging system used was the CRNet/HD-CR35 NDT Plus from DUERR, Germany. The mirror was placed on the detection table and fixed with a soft silicone pad to prevent damage caused by the movement during the detection process.

SEM-EDS

The local morphology of the bronze mirror was observed using a scanning electron microscope (Quattro ESEM, Thermo Fisher Scientific, Waltham, MA, USA) and an energy dispersive spectroscopy (Quattro ESEM EDS, Thermo Fisher Scientific, Waltham, MA, USA) at an accelerating voltage of 10–15 kV. EDS was chosen to use mapping mode to perform distribution of elements.

Micro-Raman

The patina composition was determined using a micro-Raman spectrometer (Thermo Scientific DXRxi, Thermo Fisher Scientific, USA) and an accessory microscope (OLYMPUS BX51, Olympus Corporation, Japan). The Raman excitation light was provided by a Nd: YAG laser with an excitation wavelength of 532 nm, a power of 0.5 mW, and a probe diameter of approximately 1 mm. The equipment was calibrated prior to the tests using the 520.5 cm⁻¹ line at the peak of the silicon wafer³⁷. The mirror was stably placed on the microscope stage for point-by-point observation and detection.

Electrochemical Testing. The electrochemical corrosion behavior of the bronze mirror was analyzed by a combination of open-circuit potential (OCP), electrochemical impedance spectroscopy (EIS) and potentiodynamic scanning (PDS) using an electrochemical workstation CS-100E from CorrTestTM, China. Twelve points on the mirror and decorated surfaces of the bronze mirror were tested point-by-point using a pen-probe designed in the previous work³⁸. The diameter of each test point was 2.5 mm. The reference electrode was chosen as Ag/AgCl, and the auxiliary electrode was a platinum mesh. The electrolyte was selected as an aqueous NaNO₃ solution with a mass fraction of 1.0% for OCP with EIS and of 0.5% for PDS.

After connecting the three-electrode system, the OCP could be carried out, and the measurement time was selected as 50 min. After the potential stabilized, the electrochemical impedance test could be switched on. A sinusoidal perturbation signal with an amplitude of 10 mV was tested in the range of 100 kHz~10 mHz without applying DC polarization. Potentio-dynamic polarization curves were obtained with a scanning rate of $0.5 \, \text{mV} \cdot \text{s}^{-1}$ in the potential range from $-0.1 \, \text{to} +0.1 \, \text{V}$ relative to the corrosion potential. Electrochemical data were analyzed using Zview and Cview software to obtain fitted curves and equivalent circuits.

Results

All the points were tested and analyzed in accordance with Fig. 1. The six points selected on the mirror surface had marked difference between patina

under the microscope in Fig. 2. Point M-1 and M-2 were relatively flat, and there some scratches could be seen on the surface. These two points showed a silvery and shiny effect to the naked eye, but appeared in the yellow-green color of corroded bronze under microscopic observation. The green patina at Point M-3 and M-4 showed an island-like distribution, with obvious protrusion. The Point M-5 and M-6 showed surface with blue patina. The blue patina could cover the green one, forming a stacked structure and being slightly flatter compared to the pure green patina.

Microscopic observation of the six points of the decorated surface in Fig. 2 showed that there were no scratches at Points D-1 and D-2, and the corrosion degree and the patina coverage were much greater than those on the mirror surface. The range of green patina growth on the decorated surface was much larger than the area of the blue one. The blue patina was only about 1–2 cm in diameter and grew almost completely adjacent to the smooth surface.

Comparing the peak positions of the standard refs. 39–41, as shown in Figs. 3 and 4, it could be determined that the main component of the light green patina was malachite with the characteristic peaks of 150, 179, 220, 270 and 432 cm⁻¹, and the blue patina was azurite with the peaks of 112, 177, 280 and 399 cm⁻¹. The 179 cm⁻¹ was possibly an out-of-plane bending, and the 432 cm⁻¹ was a bending mode of malachite. The 270 cm⁻¹ was an O-Cu-OH bending mode of malachite. The peak of 1091 or 1095 cm⁻¹ was assigned to the CO symmetric stretching vibration. The azurite had a band at 1575 cm⁻¹, which was attributed to the carbonate antisymmetric stretching vibration observed at 1490 cm⁻¹ in malachite. The patina composition on the mirror surface and the decorated surface were almost completely identical. From the perspective of purity and crystallinity, they basically belonged to the extremely common patina of bronze artifacts.

Figure 5 showed the microscopic details of Point M-1 and M-2 under the SEM, which appeared silver-gray and flat to the naked eye. There was no rough patina covering or accumulating on the surface, clearly presenting the metallographic phase of the bronze casting, structured into island-state of α and $\alpha+\delta$ phases 42 . Unidirectional scratches and cross scratches after polishing were present on the mirror surface, even though it has undergone a soil environment for thousands of years. Lead oxide particles were embedded in larger holes. Basically, it can be assumed that the bronze mirror was directly cast and formed, and later polished to be a bright and reflective mirror surface in ancient time.

The Point M-3 and M-4 of green patina showed two layers of different morphology under the SEM. The outer layer was relatively flat and dense, with low roughness and thin thickness. After cracking and peeling of outer layer, the inner layer of patina exposed irregular and uneven state, with a large difference in granularity and diversity in patina appearance. Point M-5 and M-6 of the blue patina on the mirror surface were still relatively rough, and the thickness was greater than that of Point M-3 and M-4, and the blue patina was more closely adjacent to the bronze matrix.

The patina on the decorated surface was still observed by SEM. The metallographic island-state structure of the cast bronze of the Point D-1 could still be vaguely seen under the SEM in Fig. 5g, as well as the corrosion product particles of lead were detached and leave sub-circular holes. The metallographic structure of Point D-2 was not clear, mainly due to the coverage by a thin, dense and continuous oxide layer. However, the whole state did not show any traces of polishing like that on the mirror surface.

The roughness of Point D-3 and D-4 of the green patina was more obvious, and there was the irregular accumulation of patina covering and uneven size of particles. However, there was no patina peeling off to expose the metal matrix. Point D-5 and D-6 had less roughness and improved flatness than the green patina. The density was also significantly better than the green area.

The difference in the contour of the corrosion patina of the decorated surface was vague and not as clear as the mirror surface. This may be related to the polishing operation of the mirror surface. The bronze substrate was flat, which can induce the patina growth with clear boundaries.

SEM-EDS was used to conduct morphology and element relationships on the mirror surface and lateral cross-section of the bronze mirror,

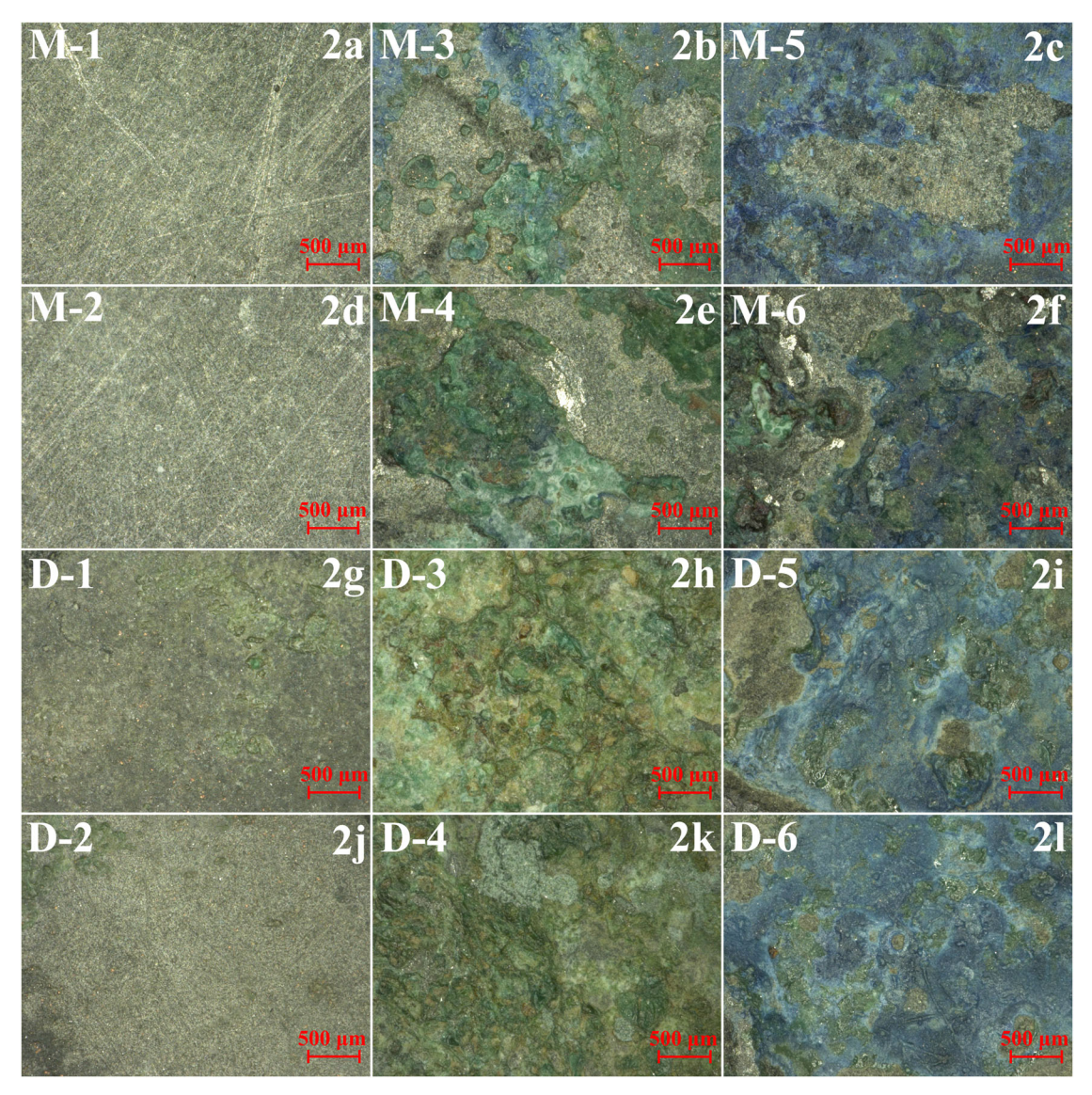


Fig. 2 | Microscopic comparisons of test points. Points on the mirror (M-) and decorated surface (D-).

respectively. Of course, the obtained elements include some trace elements in the soil components, but this analysis is mainly a quantitative study on the proportion of chief components of the bronze material and their loss situation. The bronze mirror was an alloy mainly composed of copper (Cu), tin (Sn), and lead (Pb) in Table 1. Among them, Cu was the chief component, accounting for approximately 71.99 wt.%. Next was Sn, which made up 19.76 wt.%. Tin was added to improve the hardness and luster of the bronze mirror⁴³. The third component was Pb, which was lead aimed to enhance the casting performance of bronze⁴⁴, accounting for about 3.14 wt.%. σ was the standard deviation of the obtained data, representing the distribution or dispersion of the mean value of the element data.

After being corroded in the burial environment for thousands of years, three significant changes have occurred in the proportion of element components of the mirror surface. First, the proportion of Cu at each point has decreased significantly, while the oxygen (O) has increased. Second, the proportion of Sn on the smooth area has increased, and Pb has slightly raised. Third, the signal intensity of Cu in the α phase has declined, while in the $\alpha+\delta$ eutectoid phase has become prominent.

By comparing Figs. 5 and 6, it could be found that the structures presented in the corroded areas of both the mirror surface and the cross-section were α phase (copper-based solid) and $\alpha+\delta$ eutectoid phase, and the distribution and proportion of the main elements were also quite similar

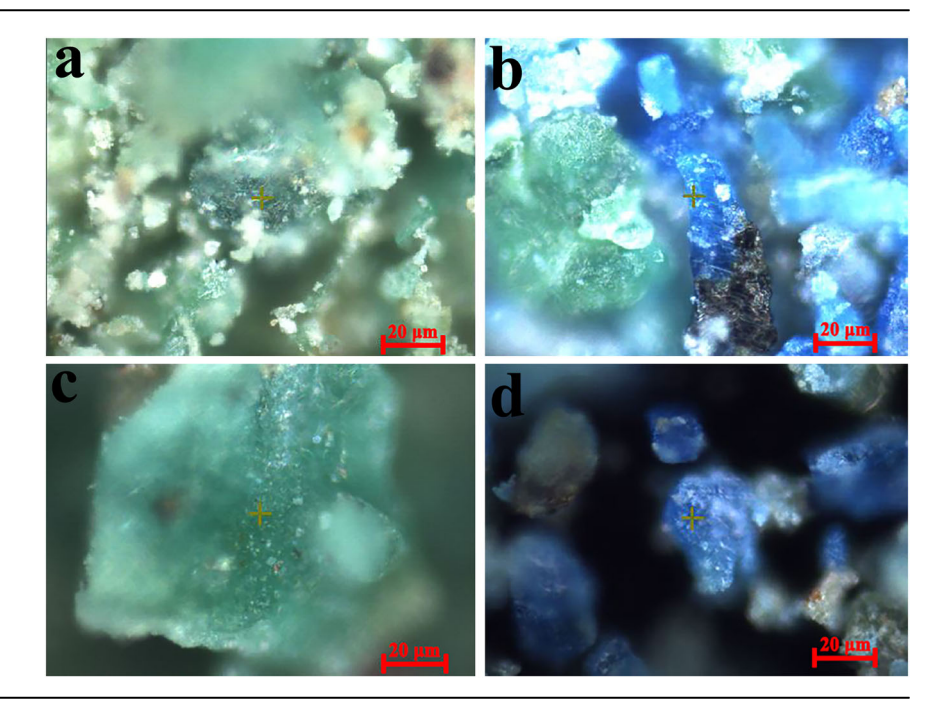
between each other. This indicated that there was no plating or coating treatment carried out on the mirror surface. Therefore, it is reasonable to speculate that there was a type of bronze mirror in the Western Han Dynasty with simple craftsmanship and no complex coating process. After natural casting and cooling, only basic grinding or polishing was required to obtain a practical bronze mirror capable of reflecting human images.

It could be seen from the two graphs in Fig. 7 that the OCP signals at the green patina on both the mirror surface (M-3, M-4) and the decorated surface (D-3, D-4) have continually exhibited potential oscillation within the testing range of 3000 s. The amplitude of the oscillation was large at the beginning, and then it gradually tended to level off within a small range about -0.17 to -0.19 V. Moreover, they both essentially stabilized at the same level as -0.19 V after 3000 s.

Within the testing time of 3000 s, the OCP measured at the two points on the blue patina of the decorated surface (D-5, D-6) exhibited an approximately parallel alignment with the abscissa in Fig. 7b. The curves were smooth, with a notably gentle slope, and the values were the highest, reaching $-0.05\,\mathrm{V}$ at the final time. This was evidence that the bronze substrate beneath the blue patina did not show the characteristics of active corrosion.

For the three types of points on the mirror surface, the OCP after 3000 s could be approximately grouped within a relatively narrow range from

Fig. 3 | Micro-morphology of the patina of the bronze mirror. The patina on the mirror (a, b) and the decorated surface (c, d).



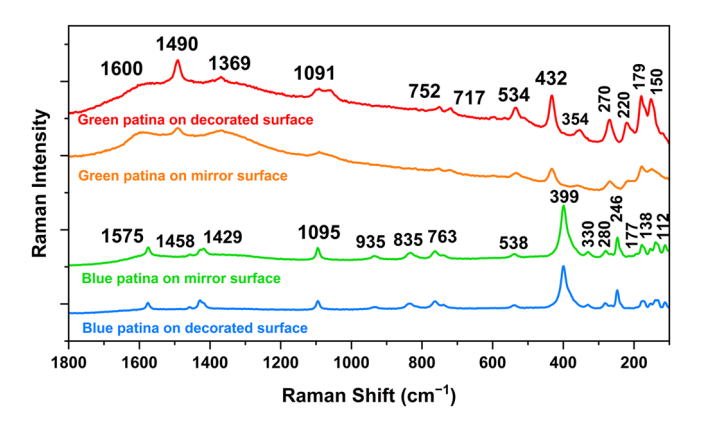


Fig. 4 | **Raman spectra of the patina.** Red and orange lines were as the Raman signals of green patina on the decorated and mirror surface. Blue and green lines were as the Raman signals of blue patina on the decorated and mirror surface.

 $-0.17~\rm V$ to $-0.19~\rm V$ in Fig. 7a. In contrast, for the decorated surface formed by casting without polishing, relatively significant differences in OCP were observed among each patina surface.

For the EIS of the smooth, green patina and blue patina of the mirror surface are shown in Fig. 8. Combined with the Nyquist and Bode plots, it can be judged that electrochemical corrosion should occur at two interfaces. According to the physical structure state of the oxidized metal, one interface was the oxidized patina located in the high-frequency region, and the other was the interface of the charge transfer layer formed between the bronze matrix and the electrolyte penetrating the oxidized patina. For the Nyquist plot of the patina layer in the high-frequency region, incomplete semicircular arcs of unequal radius were presented. It could be assumed to be formed by the internal resistance of the patina and its own capacitance effect. Under the concentration of the test electrolyte had not changed significantly. The arc radius of the real axis was determined by the internal resistance of the patina layer, and the arc height of the imaginary axis was determined by the capacitance effect.

The equivalent circuit of the EIS plots is shown in Fig. 8a, b. R_s was the mixed resistance of the electrolyte solution and the outer loose patina. R_r and CPE_r were the resistance and capacitance of the dense patina adjacent to the

metal substrate, respectively. $R_{\rm ct}$ and $CPE_{\rm dl}$ were the charge transfer resistance and double-layer capacitance of the interface between the electrolyte and the bronze.

As shown in Table 2, it could be concluded that after the mirror surface was originally polished, although it has been corroded in the soil burial environment for thousands of years, the $R_{\rm ct}$ of the silver-gray smooth area remained relatively high, which as 1.39×10^4 and 2.01×10^4 $\Omega\cdot{\rm cm}^2$. The $R_{\rm s}$ of Point M-1 on the smooth surface was 2.78×10^2 $\Omega\cdot{\rm cm}^2$, and that of Point M-2 was 2.53×10^2 $\Omega\cdot{\rm cm}^2$. Meanwhile, there was no significant difference in the order of magnitude in the corresponding $CPE_{\rm r}$ values of the mirror surface.

The internal resistance of the blue patina was all lower than that of the smooth area. The $R_{\rm r}$ of Point M-5 was $0.77\times10^2~\Omega\cdot{\rm cm}^2$, and that of Point M-6 was $0.94\times10^2~\Omega\cdot{\rm cm}^2$. In addition, the $R_{\rm ct}$ has also decreased accordingly, being $1.18\times10^4~\Omega\cdot{\rm cm}^2$ and $0.97\times10^4~\Omega\cdot{\rm cm}^2$, respectively. It could be understood that the blue patina did not adhere as firmly to the substrate as the tin-rich oxide layer, and its growth could disrupt the dense and continuous interface.

The differences in $R_{\rm r}$ and $R_{\rm ct}$ between Points M-3 and M-4 of the green patina were the most marked. The $R_{\rm r}$ of Point M-3 was $1.40\times 10^2~\Omega$ -cm², and that of Point M-4 was $3.63\times 10^2~\Omega$ -cm². Generally, the green patina was relatively loose, and the distribution of its thickness or density was rather uneven. Point M-4, where the oxidation product was thicker and denser, was closely connected to the bronze substrate. It could act as a barrier under the penetration of external corrosive electrolytes, which was beneficial for protecting the substrate and keeping the charge transfer resistance at a relatively high value of $1.47\times 10^4~\Omega$ -cm². For Point M-3, although it was also in the green patina area, the corresponding state was looser. There was even a tendency for the patina layer to peel off. Electrolytes could be easily absorbed and gradually penetrated through the patina, directly acting on the bronze interface to induce corrosion, thus resulting in a smaller obstruction to charge transfer, which was $0.80\times 10^4~\Omega$ -cm².

From the perspective of the phase angle, the three types of oxide surfaces directly presented three sets of peak curves. The phase shift curves of the smooth areas M-1 and M-2 had a relatively narrow range, with the highest absolute values and steepest slopes, which proved that the existing interface was mainly dominated by dense patina. Similarly, the phase shift curves of the green patina M-3 and M-4 had the widest range, with the lowest absolute values and gentlest slopes, indicating that the bronze

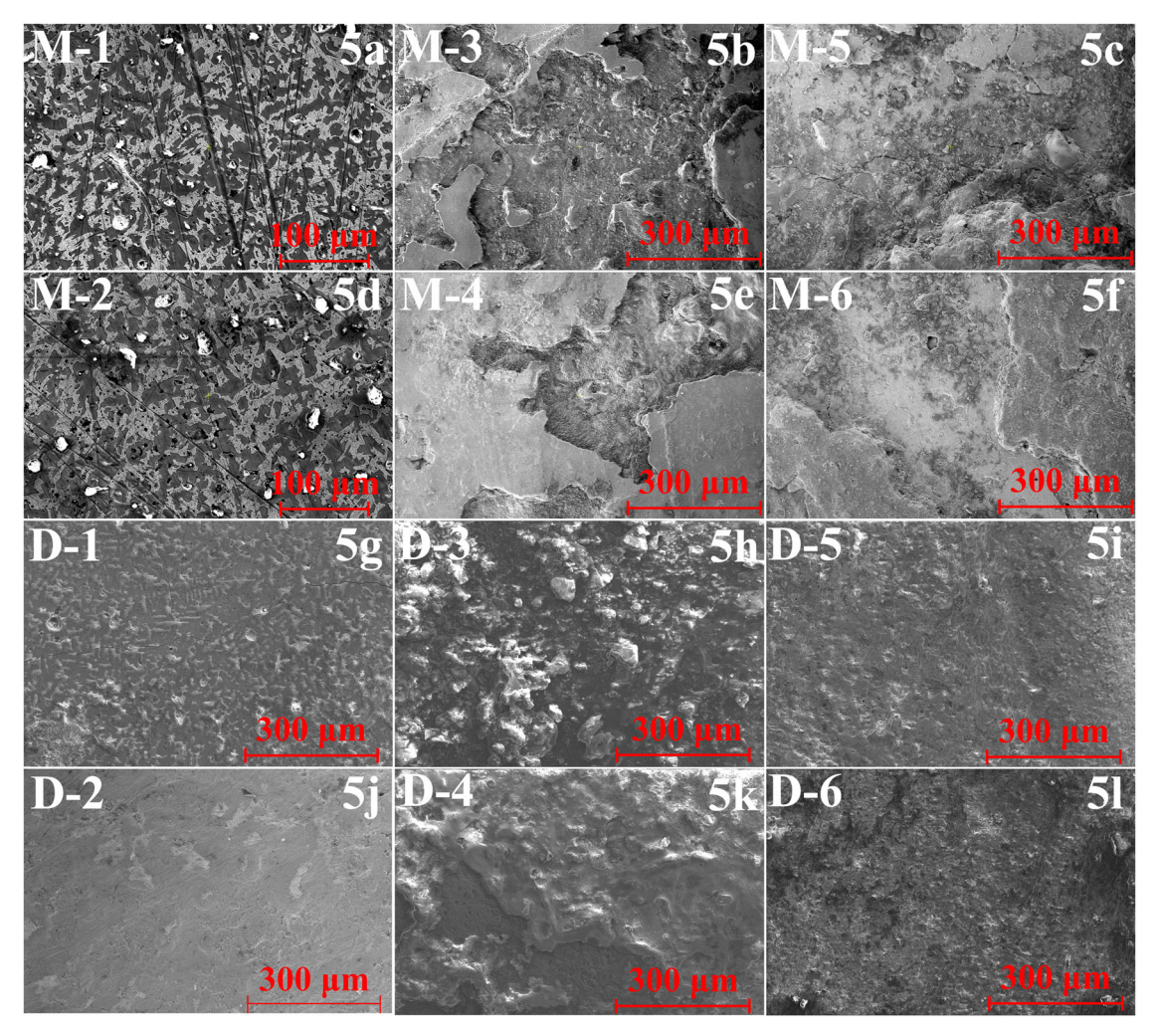


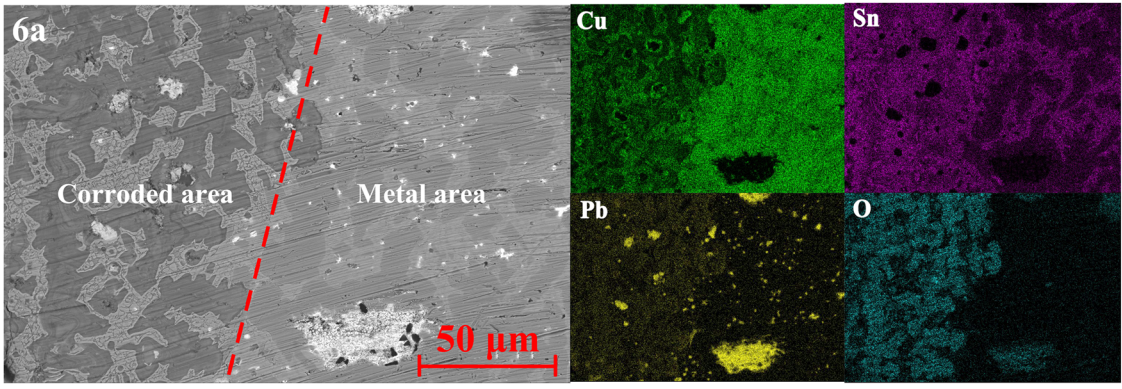
Fig. 5 | SEM of test points. Points on the mirror surface (M-) and decorated surface (D-).

Table 1 | The element composition of each point of the bronze mirror

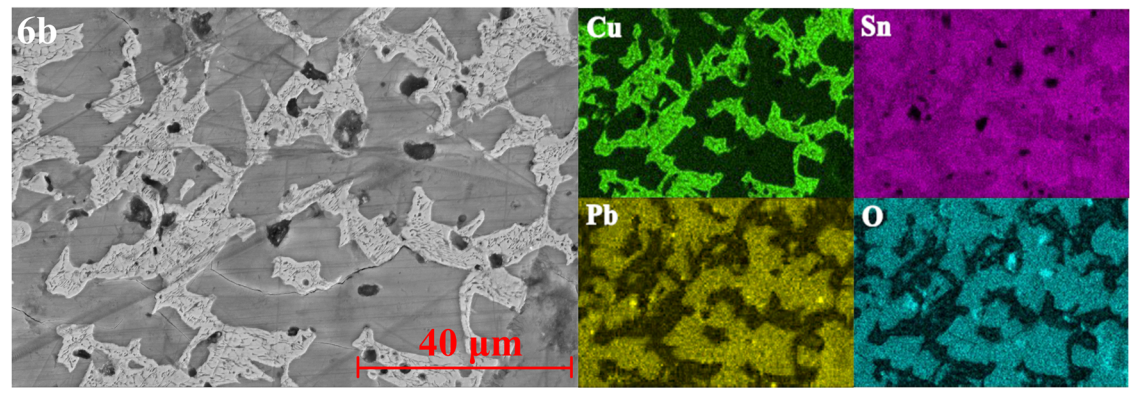
| Points | | Main element com | Main element composition (weight %) | | | | |
|-----------------------|---------------|------------------|-------------------------------------|-------------|--------------|--|--|
| | | Cu (σ) | Sn (σ) | Pb (σ) | Ο (σ) | | |
| Lateral cross-section | Metal area | 71.99 (0.19) | 19.76 (0.12) | 3.14 (0.08) | 1.85 (0.12) | | |
| | Corroded area | 31.56 (0.11) | 39.22 (0.16) | 5.96 (0.07) | 18.71 (0.09) | | |
| Mirror surface | M-1 | 30.95 (0.07) | 39.59 (0.08) | 6.64 (0.05) | 18.15 (0.08) | | |
| | M-2 | 29.76 (0.09) | 40.42 (0.08) | 7.00 (0.05) | 18.06 (0.08) | | |
| | M-3 | 43.55 (0.16) | 3.31 (0.11) | 2.90 (0.10) | 37.57 (0.15) | | |
| | M-4 | 40.82 (0.16) | 3.01 (0.12) | 2.64 (0.11) | 37.60 (0.16) | | |
| | M-5 | 41.84 (0.15) | 3.76 (0.11) | 3.01 (0.09) | 37.99 (0.15) | | |
| | M-6 | 42.47 (0.18) | 1.87 (0.13) | 2.18 (0.12) | 37.63 (0.18) | | |
| Decorated surface | D-1 | 26.10 (0.16) | 39.93 (0.17) | 5.32 (0.10) | 23.54 (0.17) | | |
| | D-2 | 29.36 (0.17) | 38.11 (0.13) | 4.98 (0.09) | 25.63 (0.15) | | |
| | D-3 | 48.63 (0.15) | 1.04 (0.09) | 2.48 (0.09) | 38.29 (0.14) | | |
| | D-4 | 47.52 (0.11) | 2.13 (0.08) | 3.66 (0.12) | 37.10 (0.16) | | |
| | D-5 | 44.63 (0.13) | 1.23 (0.08) | 2.22 (0.11) | 35.41 (0.17) | | |
| | D-6 | 45.56 (0.09) | 1.87 (0.11) | 1.85 (0.05) | 36.11 (0.18) | | |

interface had undulations with loose patina or the pits caused by oxidation were unevenly distributed. The state of blue patina was between the above two surfaces.

In contrast, the most intuitive thing was that the $R_{\rm s}$, $R_{\rm r}$ and $R_{\rm ct}$ values at the six points on the decorated surface were almost all smaller than those on the mirror surface, while both $CPE_{\rm r}$ and $CPE_{\rm dl}$ were significantly increased.

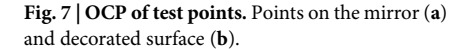


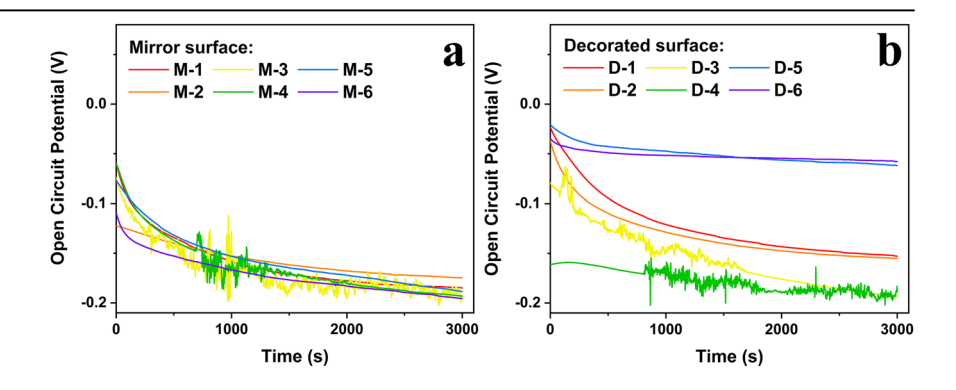
lateral cross-section



mirror surface

Fig. 6 | SEM-EDS of the bronze mirror. The lateral cross-section (a) and mirror surface (b) of the bronze mirror.





Especially on the smooth areas of the two surfaces, the difference in the $\mathit{CPE}_{\mathrm{dl}}$ values was the greatest.

The characteristics of the double-layer capacitance could generally reflect the state of the metal surface ^{46,47}. A larger capacitance value usually means that the double-layer structure between the metal and the electrolyte was relatively developed, and the effective area available for charge storage on the interface is larger. For bronze artifacts, when the corrosion interface was rough or the patina layer was thick, their double-layer capacitance would increase. Because the rough surface provided more charge-adsorption sites, and the loose patina could also easily retain the corrosive medium, enabling charges to accumulate more effectively at the interface between the metal and the electrolyte. This reflected that the decorated surface could be prone to ion enrichment and exhibited relatively high corrosion reaction activity than the mirror surface.

Furthermore, from the perspective of corrosion kinetics, the relatively fast reaction rate of metal may lead to the rapid formation of the electric double layer, resulting in a high capacitance value. This could be understood that the inhibitory effect on charge transfer of the patina close to the metal on the decorated surface was relatively weak. Compared with the mirror surface polished, the decorated surface was more prone to being induced to corrode by external electrolyte. The metal ions and anions induced by the electrolyte were highly enriched and retained at the rougher interface. This enhanced the conductive property of the interface, enabling more efficient charge transfer. As a result, the redox reaction occurred more quickly, and the corrosion state became more obvious for the decorated surface.

In potentiodynamic scanning analysis, the linear polarization and the weak polarization region were selected to characterize the bronze mirror in Fig. 9. Generally, relative to the equilibrium potential, the

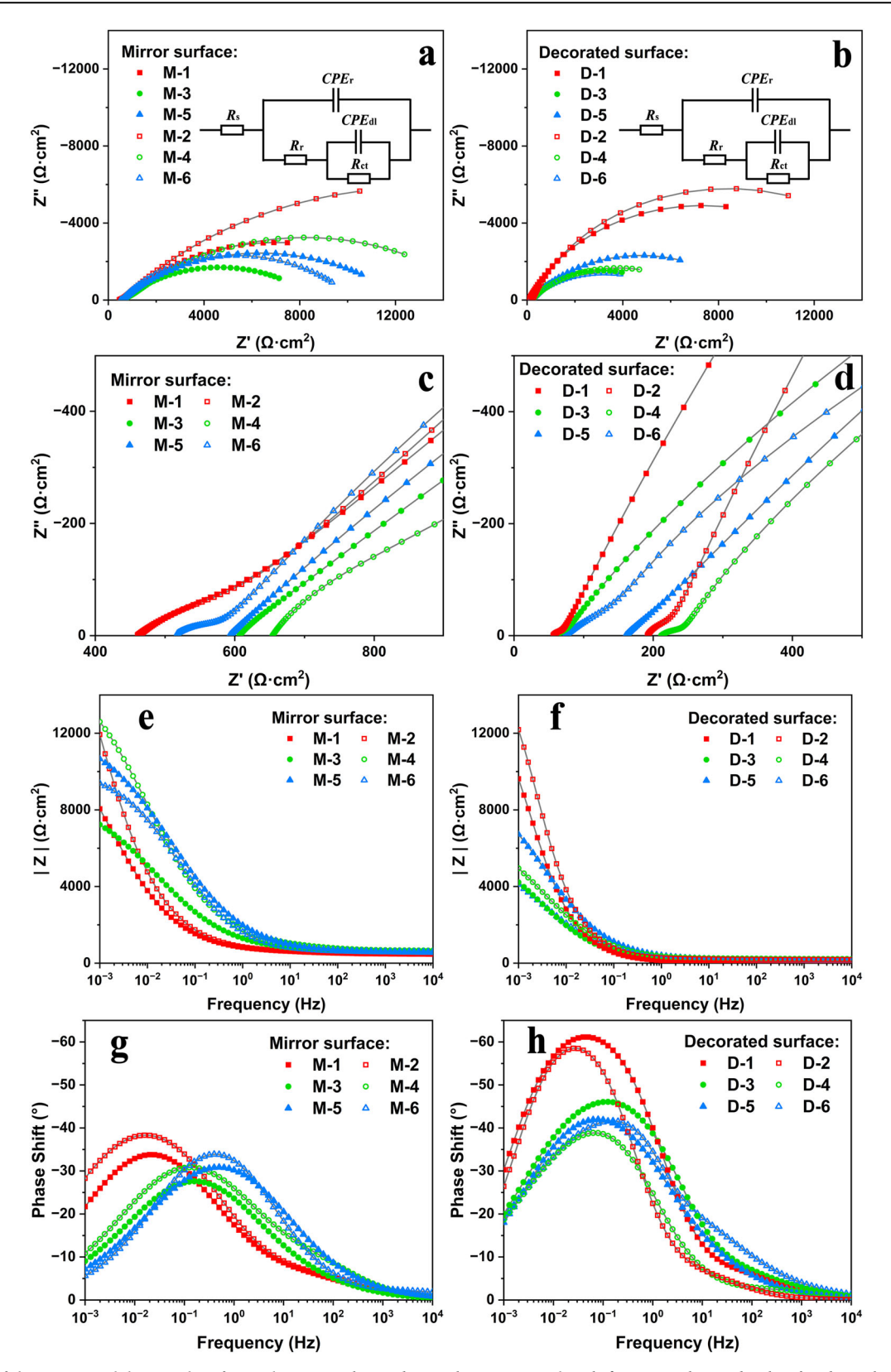


Fig. 8 | EIS plots of the mirror and decorated surface. a, b Nyquist plots and equivalent circuit; c, d High-frequency plots in detail; e, f Bode-total impedance values; g, h Bode-phase angles.

potential deviation within a few millivolts belongs to the linear polarization region, and the range within dozens of millivolts can be considered as the weak polarization region⁴⁸. Within these two regions, the system is closer to the natural equilibrium state. It can provide approximate information about the corrosion rate within a relatively short

testing time without the need for long-term monitoring⁴⁹. This avoids problems such as the changes of the bronze surface and the occurrence of side reactions that may be caused by strong polarization, and can more truly reflect kinetic parameters such as the exchange current density (I_0) and the polarization resistance (R_p). When the polarization potential is

Table 2 | Equivalent circuit fitting data of EIS plots

| Points | | $R_s \times 10^2 (\Omega \cdot cm^2)$ | $R_r \times 10^2 (\Omega \cdot cm^2)$ | R _{ct} × 10 ⁴ (Ω·cm ²) | $CPE_r \times 10^{-4} (s^n \cdot \Omega^{-1} \cdot cm^{-2})$ | n _r | $CPE_{dl} \times 10^{-4} (s^n \cdot \Omega^{-1} \cdot cm^{-2})$ | n _{dl} | χ² |
|-------------------|-----|--|--|--|--|----------------|---|-----------------|-------|
| Mirror surface | M-1 | 4.63 | 2.78 | 1.39 | 4.02 | 0.52 | 7.31 | 0.57 | 0.003 |
| | M-2 | 4.60 | 2.53 | 2.01 | 3.12 | 0.51 | 6.47 | 0.58 | 0.002 |
| | M-3 | 6.07 | 1.40 | 0.80 | 1.42 | 0.64 | 3.55 | 0.47 | 0.006 |
| | M-4 | 6.54 | 3.63 | 1.47 | 0.54 | 0.69 | 2.96 | 0.51 | 0.011 |
| | M-5 | 5.92 | 0.77 | 1.18 | 1.07 | 0.61 | 1.33 | 0.44 | 0.001 |
| | M-6 | 5.13 | 0.94 | 0.97 | 0.99 | 0.47 | 1.68 | 0.64 | 0.004 |
| Decorated surface | D-1 | 0.56 | 0.22 | 1.46 | 7.51 | 0.72 | 19.08 | 0.77 | 0.005 |
| | D-2 | 1.92 | 0.62 | 1.64 | 6.58 | 0.76 | 14.63 | 0.79 | 0.007 |
| | D-3 | 0.61 | 0.44 | 0.62 | 15.76 | 0.56 | 6.09 | 0.77 | 0.002 |
| | D-4 | 2.11 | 0.51 | 0.75 | 8.74 | 0.47 | 8.12 | 0.76 | 0.002 |
| | D-5 | 1.60 | 2.31 | 0.90 | 9.15 | 0.59 | 3.27 | 0.63 | 0.004 |
| | D-6 | 0.73 | 3.21 | 0.61 | 14.58 | 0.51 | 3.37 | 0.88 | 0.001 |

Fig. 9 | Polarization curves of test points. Points on the mirror (a) and decorated surface (b).

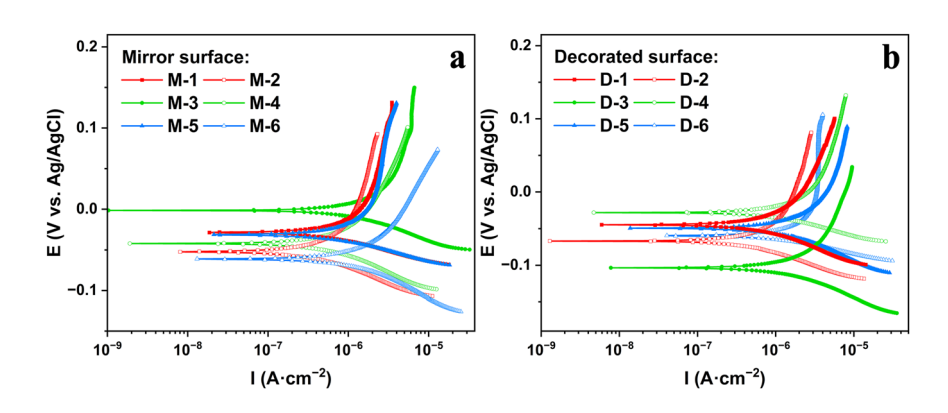


Table 3 | Fitting data of polarization curves

| Points | | $R_{\rm p} \times 10^3$ ($\Omega \cdot \rm cm^2$) | <i>I</i> ₀ × 10 ^{−6} (A·cm ^{−2}) | $E_0 \times 10^{-1}$ (V) | Corrosion rate × 10 ⁻¹ (mm⋅a ⁻¹) |
|-------------------|-----|---|---|--------------------------|---|
| Mirror surface | M-1 | 12.40 | 2.10 | -0.28 | 0.25 |
| | M-2 | 24.60 | 1.06 | -0.52 | 0.12 |
| | M-3 | 7.39 | 3.52 | -0.01 | 0.41 |
| | M-4 | 17.17 | 1.51 | -0.42 | 0.18 |
| | M-5 | 10.14 | 2.57 | -0.31 | 0.30 |
| | M-6 | 8.87 | 2.93 | -0.61 | 0.34 |
| Decorated | D-1 | 14.33 | 1.82 | -0.44 | 0.21 |
| surface | D-2 | 18.93 | 1.37 | -0.66 | 0.16 |
| | D-3 | 7.04 | 3.69 | -1.03 | 0.43 |
| | D-4 | 7.36 | 3.54 | -0.28 | 0.41 |
| | D-5 | 7.83 | 3.32 | -0.49 | 0.39 |
| | D-6 | 5.63 | 4.62 | -0.59 | 0.54 |

very small, the corrosion current is approximately equal to I_0 . In the weak polarization region, there is a close relationship between the $R_{\rm p}$ and I_0 , which can be approximately described by the Stern-Geary equation of Larger I_0 means that it has the faster the reaction rate of the local corrosion of bronze mirror under the equilibrium state, and the more likely the corrosion reaction could occur at the tested area with the smaller $R_{\rm p}$. Conversely, the smaller I_0 commonly shows the larger $R_{\rm p}$ and the stronger resistance against the corrosion I_0 .

Fitting the polarization curves respectively to obtain the $R_{\rm p}$ and I_0 in Table 3. The data results basically corresponded to the trend shown by the

 $R_{\rm ct}$ in EIS. First, overall, the corrosion potential of the mirror surface was slightly higher than that of the decorated surface. The $R_{\rm p}$ was also greater than the value of the decorated surface, and the I_0 was smaller.

In addition, the $R_{\rm p}$ on the smooth areas was significantly greater than those on the green and blue patina areas, which was consistent with the conclusion of EIS. That was to say, smooth surface exhibited better corrosion resistance, while the growth of patina could damage the interface and reduce the resistance ability. However, under the potentiodynamic scanning testing, from the perspective of $R_{\rm p}$ value, the difference between the green and the blue patina was not very remarkable. It could be understood that $R_{\rm p}$ was hardly able to analyze the electrochemical differences between patina from more perspectives, like the electrochemical impedance equivalent elements, such as the $R_{\rm s}$ and $R_{\rm cb}$ with more detailed parameters.

Discussion

The surface of bronze mirrors from archeological excavations or displayed in museum collections are generally covered with blue or green patina. There could also be a state where parts of the mirror surface appear silvergray. Although it is difficult for them to reflect human images anymore, their smooth luster is particularly remarkable. In order to explore this issue, this work took a bronze mirror of the Han Dynasty as a sample for comprehensively analyzing the correlation between macroscopic patina and the local corrosion from the perspective of in situ testing.

The metallographic structures, as well as the distribution and proportion of main elements on the surface and lateral cross-section of the bronze mirror, were quite similar. This indicated that there was no obvious post-plating or coating treatment carried out on the mirror surface. After natural cooling during casting, only basic polishing was done. When the bronze mirror was buried in natural soil, generally the $\alpha+\delta$ eutectoid phase (tin-rich phase) had a more negative potential compared to the α phase

(copper-based solid solution). It became the anode in the corrosive medium and underwent the oxidation reaction to be corroded⁴². The corrosion products, such as tin oxide, generated during this process were not easy to diffuse and relatively stable, resulting in a potential reversal with the a phase. As a result, the α phase was transformed into a new anode and was prone to losing electrons and being oxidized to form free ions^{8,23}. Meanwhile, the copper ions in the a phase could be more likely to diffuse and dissolve in the surrounding soil, and react with other anions to form corrosion products. Due to the copper and tin in the $\alpha + \delta$ phase corroding at a slower rate, they could remain and gradually accumulate locally, thus the relative proportion increasing. The oxidation products of tin could basically adhere to the bronze interface, while lead was embedded in the bronze matrix in the form of oxide particles. Therefore, on the rough and thick patina areas, the signals of tin and lead were masked by the copper patina. While on the exposed smooth areas, there was a natural phenomenon that the proportion of Sn and Pb was slightly higher.

The so-called flat and silver-gray luster areas on the mirror surface were the $\alpha+\delta$ eutectoid remaining after the loss of copper elements. The tin-rich $\alpha+\delta$ phase showed a silver color after oxidation. Under the SEM, the tin-rich $\alpha+\delta$ phase protruded more outward than the copper-based α phase, while the copper-based part had sunken due to loss, forming a local concave-convex texture. This led to the inability of light reflection to be concentrated, resulting in serious scattering. Therefore, to the naked eye, it showed flat and smooth, but cannot normally reflect clear human images. It is reasonable to speculate that there was a type of bronze mirror in the Western Han Dynasty with simple craftsmanship and no complex coating process. After natural casting and cooling, only basic grinding or polishing was required to obtain a practical bronze mirror capable of reflecting human images.

The polishing operation and the loss of copper ions could expose more surface area of the tin component to the natural environment, and form a relatively continuous and dense oxide layer. These oxidation products occupied the corrosion active sites and more strongly restricted the formation of free metal ions, having an isolating effect on external corrosion factors, which was beneficial to the protection of the bronze substrate^{53–55}. For the polished mirror surface, the uniformity of the substrate was improved. Even if different patina grew, the open-circuit potential could be ensured to converge. Overall, the corrosion potential, charge transfer resistance and polarization resistance of the mirror surface were all higher than those of the decorated surface, and the corrosion current density was relatively smaller. The patina layer on the decorated surface was relatively thick, and the morphological boundaries were rather blurred, unlike the patina on the mirror surface, which had clear contours. The loose physical structure of the patina on the decorated surface could retain or adsorb more electrolytes. The rough surface provided more charge-adsorption sites, increasing the ion concentration at the interface and enhancing the doublelayer capacitance to accelerate corrosion.

In addition, the charge transfer resistance and polarization resistance of the silver-gray smooth areas on both the mirror surface and the decorated surface were significantly greater than those of the green and blue patina areas. A polished surface could exhibit better corrosion resistance, while the growth of patina broke the resistant ability of the flat surface. The blue and green patina on the two surfaces of the bronze mirror were azurite and malachite, and there was no obvious difference in patina components between the mirror surface and the decorated surface. The green patina was more porous and looser, and the corrosion pits or unevenness on the corrosion interface were more pronounced⁵⁶. When the electrolyte met the patina, it gradually infiltrated the patina layer up to each corrosion pit under the testing area. The corrosion signals of each micro pore overlapped in the OCP, resulting in an unpredictable oscillation and making it difficult to be stable in the green patina. Azurite area coexisted with malachite, and the flatness was improved with a dense patina layer. The green and blue patina themselves had a relatively weak inhibitory effect on the transfer of electrons or ions. Instead, they could form channels for the penetration of external corrosive media into the substrate, resulting in local corrosion currents.

Therefore, compared with the smooth areas, the green and blue patina had a weaker isolating and protective effect on the bronze substrate, and its corrosion resistance was insufficient. By comparison, the area covered by green malachite should have the worst corrosion resistance among the three types of testing surfaces, and the non-uniformity and differences among points were also the greatest. It should also receive more attention in the process of conservation.

Data availability

The authors declare that the data supporting the findings of this study are available within the paper.

Received: 14 March 2025; Accepted: 4 August 2025; Published online: 18 August 2025

References

- Di Turo, F. Limits and perspectives of archaeometric analysis of archaeological metals: a focus on the electrochemistry for studying ancient bronze coins. J. Cult. Herit. 43, 271–281 (2020).
- Scott, D. A. Copper and Bronze in Art: Corrosion, Colorants, Conservation (Getty, 2002).
- Ingo, G. M. et al. Surface studies of patinas and metallurgical features of uncommon high-tin bronze artefacts from the Italic necropolises of ancient Abruzzo (Central Italy). Appl. Surf. Sci. 470, 74–83 (2019).
- Ingo, G. M. et al. Micro-chemical investigation of corrosion products naturally grown on archaeological Cu-based artefacts retrieved from the Mediterranean Sea. Appl. Surf. Sci. 470, 695–706 (2019).
- Hu, Y., Wei, Y., Li, L., Zhang, J. & Chen, J. Same site, different corrosion phenomena caused by chloride: the effect of the archaeological context on bronzes from Sujialong Cemetery, China. J. Cult. Herit. 52, 23–30 (2021).
- Pollard, A. M., Liu, R., Rawson, J. & Tang, X. From alloy composition to alloying practice: Chinese bronzes. *Archaeometry* 61, 70–82 (2019).
- Luo, Z. et al. Scientific analysis and research on the Warring States bronze mirrors unearthed from Changsha Chu cemetery, Hunan province, China. Archaeometry 64, 1187–1201 (2022).
- Oudbashi, O. Multianalytical study of corrosion layers in some archaeological copper alloy artefacts. Surf. Interface Anal. 47, 1133–1147 (2015).
- Petrasz, P. et al. Green alternatives for archaeological iron stabilization. Stud. Conserv. 69, 270–280 (2024).
- Schroder, S. A., Costantini, I., Etxebarria, I., Madariaga, J. M. & Arana, G. Assessment of marine and urban-industrial environmental impact on stone acting as the base of a quaternary bronze sculpture. *Microchem. J.* 204, 111187 (2024).
- Cofini, E. et al. The role of particulate matter in bronze corrosion: a novel method for assessment and prediction. Sci. Total Environ. 968, 178845 (2025).
- 12. Hara, S., Kamimura, T., Miyuki, H., Yamashita, M. & Uchida, H. Protective ability index of rust layer formed on weathering steel bridge. *Corros. Sci. Technol.* **6**, 128–132 (2007).
- Yucel, N., Kalkanli, A. & Caner-Saltik, E. N. Investigation of atmospheric corrosion layers on historic iron nails by micro-Raman spectroscopy. *J. Raman Spectrosc.* 47, 1486–1493 (2016).
- Hu, P. et al. Corrosion behavior of ancient white cast iron artifacts from marine excavations at atmospheric condition. Metals 12, 921 (2022).
- Couture-Rigert, D. E., Sirois, P. J. & Moffatt, E. A. An investigation into the cause of corrosion on indoor bronze sculpture. *Stud. Conserv.* 57, 142–163 (2012).
- Kwon, H. & Cho, N. In-situ non destructive investigation of contemporary outdoor bronze sculptures. Herit. Sci. 12, 167 (2024).
- Dillmann, P., Neff, D. & Feron, D. Archaeological analogues and corrosion prediction: from past to future. A review. *Corros. Eng. Sci. Technol.* 49, 567–576 (2014).

- Petitmangin, A. et al. The complex atmospheric corrosion of α/β bronze bells in a marine environment. *J. Cult. Herit.* 52, 153–163 (2021).
- Zhao, F. et al. Revealing the manufacturing and corrosion characteristics of Chinese archaeological metal arrows by nondestructive neutron techniques. *Archaeol. Anthropol. Sci.* 16, 50 (2024).
- James, B. & Hudgins, A. in Handbook of Materials Failure Analysis with Case Studies from the Oil and Gas Industry (eds Makhlouf, A. S. H. & Aliofkhazraei, M.) 1–38 (Butterworth-Heinemann, 2016).
- 21. Dowson, D. & Neville, A. in *Joint Replacement Technology* 2nd edn (ed. Revell, P. A.) 401–442 (Woodhead, 2014).
- Doménech-Carbó, A. & Doménech-Carbó, M. T. in *Electrochemistry for Cultural Heritage* (eds Scholz, F. & Péter, L.) 265–298 (Springer, 2023).
- Bernard, M. C. & Joiret, S. Understanding corrosion of ancient metals for the conservation of cultural heritage. *Electrochim. Acta* 54, 5199–5205 (2009).
- Domenech-Carbo, A. & Domenech-Carbo, M. T. Electroanalytical techniques in archaeological and art conservation. *Pure Appl. Chem.* 90, 447–461 (2018).
- Domenech-Carbo, A., Teresa Domenech-Carbo, M., Amparo Peiro-Ronda, M., Martinez-Lazaro, I. & Barrio-Martin, J. Application of the voltammetry of microparticles for dating archaeological lead using polarization curves and electrochemical impedance spectroscopy. *J. Solid State Electrochem.* 16, 2349–2356 (2012).
- Hernandez-Escampa, M., Gonzalez, J. & Uruchurtu-Chavarin, J. Electrochemical assessment of the restoration and conservation of a heavily corroded archaeological iron artifact. *J. Appl. Electrochem.* 40, 345–356 (2010).
- Domenech, A. Tracing, authenticating and dating archaeological metal using the voltammetry of microparticles. *Anal. Methods* 3, 2181–2188 (2011).
- Di Turo, F. et al. A multi-analytical approach for the validation of a jellified electrolyte: application to the study of ancient bronze patina. *Microchem. J.* 134, 154–163 (2017).
- Ramirez Barat, B., Crespo, A., Garcia, E., Diaz, S. & Cano, E. An ElS study of the conservation treatment of the bronze sphinxes at the Museo Arqueologico Nacional (Madrid). J. Cult. Herit. 24, 93–99 (2017).
- Di Turo, F. et al. PVA hydrogel as polymer electrolyte for electrochemical impedance analysis on archaeological metals. *J. Cult. Herit.* 37, 113–120 (2019).
- Salem, Y., Oudbashi, O. & Eid, D. Characterization of the microstructural features and the rust layers of an archaeological iron sword in the Egyptian Museum in Cairo (380-500 AD). *Herit. Sci.* 7, 19 (2019).
- 32. Liu, S. et al. Optimizing the thermal treatment for restoration of brittle archaeological silver artifacts. *Herit. Sci.* **10**, 21 (2022).
- Figueiredo, E., Silva, R. J. C., Araujo, M. F. & Senna-Martinez, J. C. Identification of ancient gilding technology and Late Bronze Age metallurgy by EDXRF, Micro-EDXRF, SEM-EDS and metallographic techniques. *Microchim. Acta* 168, 283–291 (2010).
- Quaranta, M., Catelli, E., Prati, S., Sciutto, G. & Mazzeo, R. Chinese archaeological artefacts: microstructure and corrosion behaviour of high-leaded bronzes. J. Cult. Herit. 15, 283–291 (2014).
- 35. Wang, Y. P., Long, S. S., Wang, X. N., Liu, F. Z. & Ma, Q. L. New insights on the analysis of the causes of glossy lustre on the surface of ancient Chinese bronze mirrors. *Herit. Sci.* **12**, 136 (2024).
- Liang, J. & Parker, Q. Close up to the surface: reflections on a preliminary forensic study of four Chinese bronze mirrors. *Herit. Sci.* 9, 25 (2021).
- Vandenabeele, P. An alternative macro-Raman mapping algorithm, adapting the numbers of accumulations. *J. Raman Spectrosc.* 55, 1067–1079 (2024).

- Jia, M., Hu, P. & Hu, G. An easy-to-assemble probe for in situ corrosion testing of archaeological metal. *Electrochem. Commun.* 147, 107427 (2023).
- 39. Colomban, P., Tournie, A., Maucuer, M. & Meynard, P. On-site Raman and XRF analysis of Japanese/Chinese bronze/brass patina—the search for specific Raman signatures. *J. Raman Spectrosc.* **43**, 799–808 (2012).
- Frost, R. L., Martens, W. N., Rintoul, L., Mahmutagic, E. & Kloprogge, J. T. Raman spectroscopic study of azurite and malachite at 298 and 77 K. J. Raman Spectrosc. 33, 252–259 (2002).
- Yu, B. S., Fang, J. N. & Huang, E. P. Characteristics of the Raman spectra of archaeological malachites. *J. Raman Spectrosc.* 44, 630–636 (2013).
- 42. Saraiva, A. S., Figueiredo, E., Aguas, H. & Silva, R. J. C. Characterisation of archaeological high-tin bronze corrosion structures. *Stud. Conserv.* **67**, 222–236 (2022).
- 43. Srinivasan, S. Megalithic and continuing peninsular high-tin binary bronzes: possible roots in Harappan binary bronze usage? *Trans. Indian Inst. Met.* **66**, 731–737 (2013).
- Artioli, G. et al. The tin content of lead inclusions in ancient tin-bronze artifacts: a time-dependent process? *J. Appl. Crystallogr.* 57, 700–706 (2024).
- Lazanas, A. C. & Prodromidis, M. I. Electrochemical impedance spectroscopy—a tutorial. ACS Meas. Sci. Au 3, 162–193 (2023).
- 46. Lasia, A. *Electrochemical Impedance Spectroscopy and its Applications* (Springer, 2014).
- Martin, M. & Lasia, A. Influence of experimental factors on the constant phase element behavior of Pt electrodes. *Electrochim. Acta* 56, 8058–8068 (2011).
- Laleh, M., Pathirana, M. & Tan, M. Y. Site-specific local polarisation curve measurements for probing localised corrosion and inhibition. *Corros. Sci.* 214, 111019 (2023).
- 49. Ijsseling, F. P. Application of electrochemical methods of corrosion rate determination to systems involving corrosion product layers. 1. Linear-polarization resistance measurement as an example of a simple method that can be performed with commercially available instruments. *Br. Corros. J.* 21, 95–101 (1986).
- Stern, M. & Geary, A. L. Electrochemical polarization: I. A theoretical analysis of the shape of polarization curves. *J. Electrochem. Soc.* 104, 56 (1957).
- Mansfeld, F. Fundamental aspects of the polarization resistance technique
 —the early days. J. Solid State Electrochem. 13, 515–520 (2009).
- Chen, L. & Su, R. K. L. Corrosion rate measurement by using polarization resistance method for microcell and macrocell corrosion: theoretical analysis and experimental work with simulated concrete pore solution. *Constr. Build. Mater.* 267, 121003 (2021).
- 53. Wu, J., Wu, Y., Wang, J. & Luo, W. Photo-induced passivation: a new corrosion mitigation strategy for bronze artefacts. *Corros. Sci.* **239**, 112401 (2024).
- 54. Taube, M., King, A. H. & Chase, W. T. Transformation of ancient Chinese and model two-phase bronze surfaces to smooth adherent patinas. *Phase Transit.* **81**, 217–232 (2008).
- Gao, T., Wu, Y. & Wang, J. Mechanism of incipient annular corrosion of high-tin bronze in simulated soil solution. *Corros. Eng. Sci. Technol.* 58, 464–474 (2023).
- Ha, H., Taxen, C., Cong, H. & Scully, J. R. Effect of applied potential on pit propagation in copper as function of water chemistry. *J. Electrochem. Soc.* 159, C59–C73 (2012).

Acknowledgements

This research was supported by the National Social Science Fund of China–Special Project of Unpopular Extinctive Subjects (No. 24VJXG033); Project of Key Laboratory of Archaeological Sciences and Cultural Heritage (No. S20250410).

Author contributions

M.J. completed the article writing and the experiment design; H.X. performed the data collection and plotting; P.H. participated in the electrochemical experiments and plotting; G.H. was responsible for the experiment design and project management. All authors reviewed and approved the article.

Competing interests

The authors declare no competing interests.

Additional information

Correspondence and requests for materials should be addressed to Gang Hu.

Reprints and permissions information is available at http://www.nature.com/reprints

Publisher's note Springer Nature remains neutral with regard to jurisdictional claims in published maps and institutional affiliations.

Open Access This article is licensed under a Creative Commons Attribution-NonCommercial-NoDerivatives 4.0 International License, which permits any non-commercial use, sharing, distribution and reproduction in any medium or format, as long as you give appropriate credit to the original author(s) and the source, provide a link to the Creative Commons licence, and indicate if you modified the licensed material. You do not have permission under this licence to share adapted material derived from this article or parts of it. The images or other third party material in this article are included in the article's Creative Commons licence, unless indicated otherwise in a credit line to the material. If material is not included in the article's Creative Commons licence and your intended use is not permitted by statutory regulation or exceeds the permitted use, you will need to obtain permission directly from the copyright holder. To view a copy of this licence, visit http://creativecommons.org/licenses/bync-nd/4.0/.

© The Author(s) 2025